

Compact H II Regions as Clocks of Massive-Star Formation: Evidence for Long Formation Timescales

PAOLO PADOAN  ^{1,2} AND MARK GIELES  ^{3,4,5}

¹Department of Physics and Astronomy, Dartmouth College, Hanover, NH, USA

²Institut de Ciències del Cosmos (ICCUB), Universitat de Barcelona (UB), Spain

³Institut de Ciències del Cosmos (ICCUB), Universitat de Barcelona (UB)

⁴Catalan Institute of Research and Advanced Studies (ICREA), Barcelona, Spain

⁵Institut d'Estudis Espacials de Catalunya (IEEC), Barcelona, Spain

Submitted to ApJL

ABSTRACT

We revisit the luminosity function (LF) of compact H II regions in the context of the inertial–inflow model, in which massive stars assemble over extended, mass-dependent timescales. The comparison of the compact-H II-region LF with that of OB stars is traditionally used to estimate the compact-H II-phase lifetime and is often cited as evidence for the classical “lifetime problem” of H II regions. We show that once stellar growth during the ionizing phase is included, the LF comparison instead constrains massive-star formation timescales, so the lifetime problem turns into evidence for prolonged growth. We illustrate the principle with a simple analytic model and then forward-model the two LFs with Monte Carlo realizations. We also derive revised Galactic LFs for compact H II regions and OB stars from the Red MSX Source survey and the Alma Luminous Star catalogue. The joint LF constraints imply a growth law where the formation time is about 2 Myr for a $60 M_{\odot}$ star, with a square-root dependence on mass. The revised OB-star LF exhibits a statistically significant knee at $\log_{10}(L_k/L_{\odot}) = 5.0$, while the H II-region LF knee occurs at lower luminosity, as expected in the interpretation that H II regions are powered by stars that are still growing in mass. We conclude that massive stars in the Milky Way form over Myr timescales that increase with their final mass.

Keywords: star formation — massive stars — H II regions — interstellar medium — Milky Way

1. INTRODUCTION

Massive stars are rare and short-lived, yet they dominate the radiative and mechanical feedback that regulates the interstellar medium and they control the chemical evolution of galaxies. Because they contribute most of the UV/optical light of star-forming systems, interpretations of distant galaxies depend sensitively on how massive stars form and evolve. Recent JWST spectroscopy of galaxies at $z \gtrsim 11$ showing unusually high nitrogen abundances (e.g. A. J. Bunker et al. 2023; M. Castellano et al. 2024; R. P. Naidu et al. 2025) may even hint at an early role for supermassive stars (C. Charbonnel et al. 2023; S. Ebihara et al. 2026), only $\simeq 300$ Myr after the Big Bang. Despite their importance, the assembly of massive stars remains poorly understood.

In cold molecular gas the thermal Jeans mass is $\sim 1 M_{\odot}$, so forming stars with $m \gtrsim 20\text{--}100 M_{\odot}$ requires sustained mass transport from larger scales, increasingly shaped by feedback once the protostar becomes luminous and photoionizes its surroundings. Compact H II regions (including hypercompact and ultracompact ob-

jects) mark the onset of this feedback while the system is still embedded.

Historically, compact H II regions were treated mainly as a by-product of massive-star formation, and their demographics were used to infer their lifetimes. In a uniform medium an H II region at $T \simeq 10^4$ K expands at roughly the ionized sound speed and should leave the compact regime ($R \lesssim 0.1$ pc) in $\sim 10^4$ yr, yet lifetimes of $\sim 10^5$ yr are inferred from a comparison of the number of H II regions to the number of OB stars, the classical “lifetime problem” (e.g. D. O. S. Wood & E. Churchwell 1989a,b; E. Churchwell 2002). Many mechanisms were proposed to prolong the compact phase (e.g. D. Hollenbach et al. 1994; E. Keto 2002; T. Peters et al. 2010; R. Galván-Madrid et al. 2011).

A widely used quantitative estimate was derived by J. C. Mottram et al. (2011, hereafter M11), who compared the compact-H II-region luminosity function (LF) from the Red MSX Source (RMS) survey (J. S. Urquhart et al. 2008; J. C. Mottram et al. 2011; S. L. Lumsden et al. 2013) with the OB-star LF (B. C. Reed 2005). Assuming the embedded ionizing star has already reached

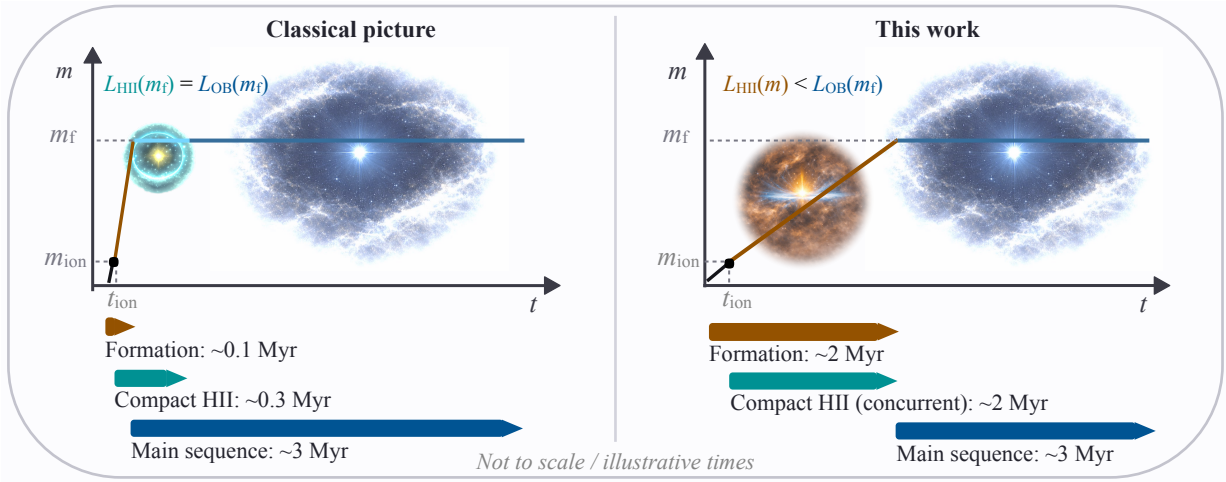


Figure 1. Schematic illustration of the mass growth and luminosity mapping assumed in the classical interpretation of compact H II regions (left) and in the IIM picture explored in this work (right). In both panels the stellar mass m increases with time until it reaches the final mass m_f , after which the star evolves on the main sequence (horizontal segment). Ionising emission turns on when the growing star crosses the threshold mass m_{ion} at t_{ion} (dot). *Classical picture*: the formation phase is short, and the compact-H II stage is treated as a subsequent, comparatively brief phase of roughly fixed stellar mass, so that the embedded ionising source is effectively already at m_f and $L_{\text{HII}}(m_f) = LOB(m_f)$. *This work*: the compact-H II phase occurs during continued accretion; the ionised emission is produced while $m < m_f$, implying $L_{\text{HII}}(m) < LOB(m_f)$ and motivating a comparison between the compact-H II-region LF at luminosity L and the OB-star LF at higher luminosities corresponding to the eventual m_f . The coloured bars indicate approximate timescales for our reference $m_f \simeq 60 M_{\odot}$ case inferred in this work; they are not to scale and are intended to illustrate the ordering of phases, highlighting that in the growth scenario the compact-H II-region phase is concurrent with the stellar mass assembly.

its main-sequence luminosity, the ratio of LFs at fixed L gives the H II-region lifetime normalized to the main-sequence lifetime,

$$t_{\text{HII}}(L) = t_{\text{MS}}(L) \frac{\phi_{\text{HII}}(L)}{\phi_{\text{OB}}(L)}. \quad (1)$$

M11 obtained $t_{\text{HII}} \sim 3 \times 10^5$ yr, reinforcing the lifetime problem; this value remains commonly adopted (e.g. T. Nony et al. 2024).

The key M11 assumption—that massive stars are essentially fully formed when the embedded ionizing phase begins—matches the classical view that massive-star formation proceeds on approximately a core-collapse timescale, $\sim 10^5$ yr (C. F. McKee & J. C. Tan 2002, 2003). In this work we adopt another view on massive star formation, leading us to a different interpretation of the nature of H II regions.

In the inertial-inflow model (hereafter IIM; P. Padoan et al. 2020, hereafter P20), massive-star assembly extends to $\sim 10^6$ yr and the compact-H II phase is powered by a star that is still accreting (Figure 1). The appropriate LF comparison is therefore not at fixed luminosity, but between $\phi_{\text{HII}}(L)$ and the OB-star LF at higher luminosity, $\phi_{\text{OB}}(L')$ with $L' > L$, which increases the inferred $t_{\text{HII}}(L)$ relative to equation (1). In this picture the longer age is not problematic: compact H II regions trace photoionized, evaporating layers of accreting structures continuously replenished by inflow

rather than pressure-driven Strömgren spheres in a uniform medium. Here we show that the joint shapes of the compact-H II-region and OB-star LFs constrain the massive-star formation time and its dependence on final mass in the IIM.

2. THE INERTIAL-INFLOW FRAMEWORK

In this work we adopt the IIM for the origin of massive stars, introduced in P20 and recently applied to globular-cluster formation in M. Gieles et al. (2025). The main features of the model needed for this work are briefly summarized in the following.

In the IIM, massive stars are assembled by large-scale converging flows that are part of the turbulent velocity field of the star-forming cloud. These flows feed the protostar (through a circumstellar disc) from an extended, turbulent, generically unbound “inflow region” of parsec size. The accretion history of a star is therefore controlled primarily by the statistics of the turbulent velocity field on the scale of its mass reservoir, not by the gravitational focusing of the star itself (contrary to competitive accretion; I. A. Bonnell et al. 2001a,b).

A key result in P20 is that the average time to reach the final stellar mass, t_{form} , increases systematically with the final stellar mass m_f as

$$t_{\text{form}}(m_f) = \tau_0 \left(\frac{m_f}{m_0} \right)^\alpha, \quad (2)$$

where m_0 is a reference mass and τ_0 is the corresponding formation time. The exponent α is considered to be a universal property of supersonic turbulence related to the velocity scaling, while τ_0 may vary with environment.

P20 find that the accretion rate, controlled by the inertial inflow, for an individual star is primarily stochastic, with no strong secular trend with time. This motivates a linear time-averaged growth law,

$$m(t; m_f) \simeq m_f \frac{t}{t_{\text{form}}(m_f)}, \quad 0 \leq t \leq t_{\text{form}}(m_f). \quad (3)$$

We will refer to equations (2) and (3) as the *growth law* and to α and τ_0 as the *growth-law parameters*.

Because the inflows that feed massive stars are generated by the turbulent cascade on scales up to the cloud (or “outer”) scale, the IIM also predicts a natural upper limit to the stellar mass, m_{max} , that turns out to be simply proportional the total cloud mass, M ,

$$m_{\text{max}} \simeq \varepsilon_{\text{max}} M, \quad (4)$$

with a dimensionless efficiency $\varepsilon_{\text{max}} \simeq 2.5 \times 10^{-3}$ expected to be a universal flow property in supersonic turbulence. An important consequence of equation (4) is the steepening of the upper end of the stellar initial-mass function (IMF) of field stars, above a knee mass $m_k = \varepsilon_{\text{max}} M_k$, where M_k is the minimum mass of star-forming clouds (see Appendix A). We will therefore model the field IMF as a broken power law, which we will characterize with three parameters: a low-mass slope s (corresponding to the IMF slope in individual clouds, for example the Salpeter value $s = 2.35$), a high-mass slope s_f (with $s_f > s$), and a knee mass m_k .

We will take equations (2) and (3) and a broken-power-law IMF as the working definition of the IIM adopted to compute the OB-star and compact-H II-region LFs.

3. PREDICTED LUMINOSITY FUNCTION SLOPES

We start with an idealised analytical derivation of the slopes of the LFs of OB stars, $\phi_{\text{OB}}(L)$, and compact H II regions, $\phi_{\text{H II}}(L)$, that will be compared with the power-law fits of the observed LFs in the next section. This derivation illustrates how the growth-law is constrained by the LF slopes.

To connect the IMF to $\phi_{\text{OB}}(L)$ we only need to specify the relations between mass and luminosity and between mass and main-sequence lifetime. We express them as power laws with effective exponents γ and δ such that $L \propto m^\gamma$ and $t_{\text{MS}} \propto m^{-\delta}$ over the luminosity range of interest. To connect the IMF to $\phi_{\text{H II}}(L)$, we further assume that compact H II regions correspond to the phase when a star is still accreting according to our growth law (see Fig. 1), and has reached a mass larger than a

threshold, m_{ion} , above which it emits a significant ionizing flux. A schematic view of this construction, from the growth tracks in the L - t plane to the resulting projections into the LFs, is shown in Fig. 2.

Throughout this work, the exponents $(s, s_f, \gamma, \delta, \alpha)$ are defined as positive numbers, while for the LFs we follow the usual convention $\phi_{\text{OB}}(L) \propto L^{\beta_{\text{OB}}}$ and $\phi_{\text{H II}}(L) \propto L^{\beta_{\text{H II}}}$, so that declining LFs have negative slopes β_{OB} and $\beta_{\text{H II}}$. We work with LFs per unit of volume and per dex in L , $\phi(L) \equiv dN/d\log_{10} L$ in units of stars $\text{kpc}^{-3} \text{dex}^{-1}$.

3.1. OB-star LF from the IMF

For clarity, we first consider a single-slope IMF for the final masses m_f ,

$$\xi(m_f) = \frac{dN}{dm_f} \propto m_f^{-s}. \quad (5)$$

The effect of a high-mass steepening (Appendix A) can be mimicked by using different effective slopes in the relevant luminosity ranges.

In a statistical steady state with a constant star-formation rate and a time-independent IMF, the number density of OB stars on the main sequence reflects the IMF weighted by their lifetimes. The space density per unit mass is

$$n_{\text{OB}}(m) \propto \xi(m_f) t_{\text{MS}}(m_f) \propto m_f^{-s-\delta}. \quad (6)$$

Per dex in mass this becomes

$$\frac{dn_{\text{OB}}}{d\log m_f} \propto m_f n_{\text{OB}}(m_f) \propto m_f^{1-s-\delta}. \quad (7)$$

Using $m_f \propto L^{1/\gamma}$ then gives a power-law OB LF of the form

$$\phi_{\text{OB}}(L) \propto L^{\beta_{\text{OB}}}, \quad \beta_{\text{OB}} = \frac{1-s-\delta}{\gamma}, \quad (8)$$

which can be applied separately to both the Salpeter’s mass range with $s \simeq 2.35$ and the steeper mass range above m_k with $s = s_f$ (equation (A6)).

3.2. Compact H II region LF from the IMF

To derive $\phi_{\text{H II}}(L)$ from the single-slope IMF we adopt the growth law from equation (3), which gives a linear-in-mass track $m(t; m_f)$ with a total duration $t_{\text{form}}(m_f)$. Because the luminosity increases along this track, the compact-H II-region LF is obtained by counting, for each m_f , the time spent in a given luminosity bin after the onset of ionization, and then integrating over the IMF; in this sense, each luminosity bin in $\phi_{\text{H II}}(L)$ mixes contributions from stars with a range of final masses (Fig. 2). The resulting LF is

$$\phi_{\text{H II}}(L) \propto L^{\beta_{\text{H II}}}, \quad \beta_{\text{H II}} = \frac{1+\alpha-s}{\gamma}, \quad (9)$$

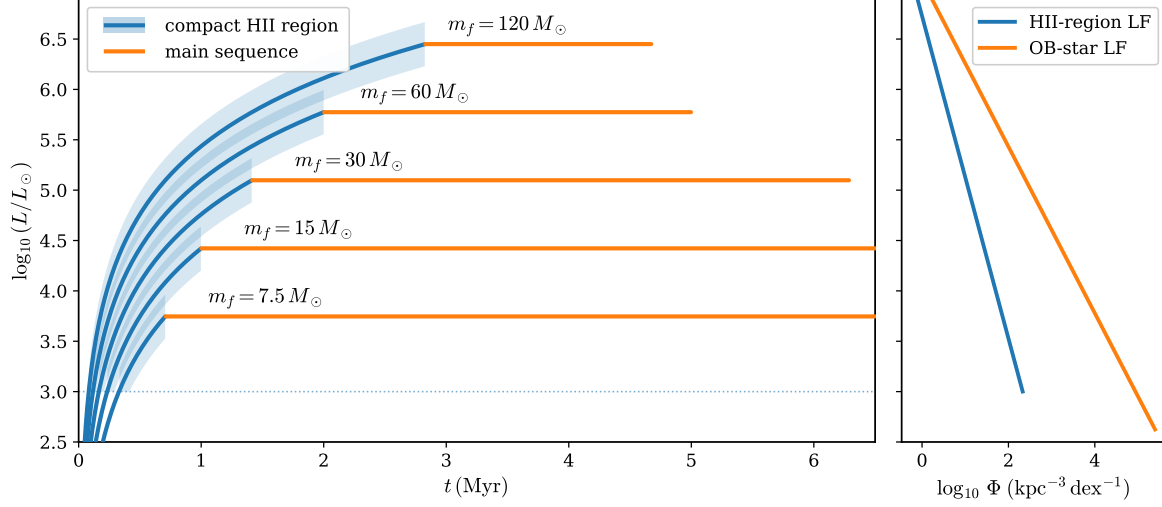


Figure 2. Schematic mapping between stellar growth tracks in the luminosity–time plane and the observed LFs in the IIM. *Left:* example evolutionary tracks for stars of different final masses m_f . During the growth phase (blue), the luminosity increases as the star accretes; once the ionization threshold is reached (dotted horizontal line at $\log_{10}(L/L_\odot) = 3$), the source is counted as a compact H II region (blue shading) while it continues to brighten. After growth ends, the star enters the main-sequence phase (orange) at approximately fixed luminosity. *Right:* the compact-H II-region and OB-star LFs (shown here schematically, in the same style as Fig. 5) can be viewed as projections of the track distribution: the H II-region LF counts the time spent in each luminosity bin *along the shaded portions of all tracks*, so a single luminosity bin receives contributions from a range of m_f ; in contrast, the OB-star LF counts the main-sequence lifetime at the luminosity corresponding to the final mass. This figure is intended purely to illustrate the geometric origin of the LF construction in the model (not to provide a quantitative fit).

(see derivation in Appendix B).

Using the the OB–star result (equation 8), the difference btween the two slopes is

$$\Delta\beta = \beta_{\text{H II}} - \beta_{\text{OB}} = \frac{\alpha + \delta}{\gamma}, \quad (10)$$

so $\phi_{\text{H II}}$ is always shallower (less negative β) than ϕ_{OB} , as long as $\alpha > -\delta$, that is for any growth law in which the overall formation time is not very strongly decreasing with final stellar mass. Equation (10) is a central analytic result of our model: irrespective of the IMF slope (s cancels out in the equation) *the difference between the compact H II-region and OB-star LF slopes provides an observational constraint on the exponent of the growth law of massive stars.*

4. THE OBSERVATIONAL LUMINOSITY FUNCTIONS

We derive updated LFs for OB stars and compact H II regions from modern catalogues, using a common methodology that allows a consistent relative normalisation. We convert source counts to a LF, $\Phi(L)$, expressed as a number density per logarithmic luminosity interval in units of $\text{kpc}^{-3} \text{dex}^{-1}$. To do so, we assume an exponential vertical distribution about the Galactic mid-plane with scale height $h = 39 \text{ pc}$ (the value inferred by M11 for H II-regions) for both compact H II regions and OB stars, given their common birth environment (they are different phases of the same objects).

To maximise the number of objects retained from the available catalogues, we include OB stars and compact H II regions out to heliocentric distances of 6 and 18 kpc, respectively. This choice necessitates luminosity-dependent completeness corrections, which we derive with an empirical effective-volume correction (see Appendix C.1). In addition, the absolute normalisation of the LFs can vary with Galactocentric radius due to large-scale structure in the star-forming disc, so in our Monte-Carlo modeling we will place the two LFs on a common effective Galactic volume scale to enable a meaningful relative normalisation (see details in Appendix C.2).

4.1. The OB-star LF from the ALS III Catalog

We derive the OB-star LF using the third release of the Alma Luminous Star catalogue (ALS III; M. Pantaleoni González et al. 2025, building on B. C. Reed 2003; M. Pantaleoni González et al. 2021) cross-matched to *Gaia* DR3 (*Gaia* Collaboration et al. 2023) and to the Galactic O-Star (GOS) catalogue (J. Maíz-Apellániz et al. 2004). The selection criteria and the derivation of bolometric luminosities are described in the Appendix D. The resulting LF, with the completeness correction described in Appendix C, is shown in the left panel of Figure 3 (blue circles with 1σ Poisson error bars) together with the OB LF of M11 (grey squares). The latter has been rescaled from $h = 45 \text{ pc}$ adopted in B. C. Reed (2005) to $h = 39 \text{ pc}$ adopted here. Our ALS III LF contains a total of 7,191 stars

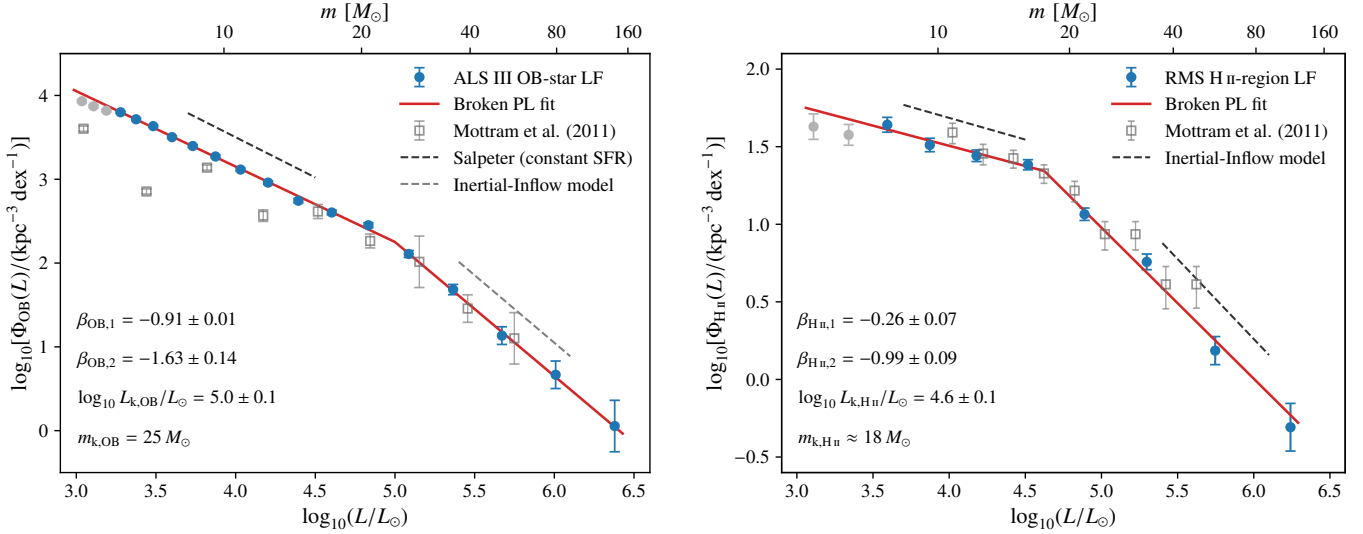


Figure 3. *Left:* OB-star LF from the ALS III catalog (blue circles with 1σ error bars) for $d \leq 6$ kpc. The lower axis shows the bolometric luminosity, and the upper axis gives the corresponding main-sequence mass using the $L(m)$ relation (see Section 4.1 for details). Number densities assume an exponential vertical distribution with scale height $h = 39$ pc. The M11 LF (gray squares) has been rescaled from $h = 45$ pc used in B. C. Reed (2005) to $h = 39$ pc for comparison. The solid line shows a continuous broken power-law fit excluding the three lowest-luminosity bins (in light gray), with best-fit values given in the inset. The dashed black and gray segments indicate reference slopes corresponding to a Salpeter IMF with constant star-formation rate and to our IIM (Sect. 3.1). *Right:* Compact H II-region LF derived from the RMS survey (blue circles with 1σ error bars). The LF from M11 is also shown (open squares), as well as a broken power-law fit (red line) excluding the first two bins (in light gray). The black dashed lines show the slopes predicted by the IIM for Salpeter's slope $s = 2.35$, growth-law index $\alpha = 0.5$, and average $L(m)$ relations at masses below and above the knee (see Sect. 3.2 for details).

with $\log_{10}(L/L_\odot) \geq 3.2$ and $d \leq 6$ kpc (9,607 including the first three low- L bins that are not used in this work), compared with approximately 490 stars in the Reed/M11 LF, estimated from the counts in B. C. Reed (2005) excluding the lowest- L bin shown in the left panel Figure 3. Despite the very different input catalogues and methodology, the two LFs agree reasonably well.

We fit the binned data in $\log_{10}\Phi_{\text{OB}}$ versus $\log_{10}L$ with a piecewise linear relation, equivalent to the broken power-law form

$$\Phi_{\text{OB}}(L) = \begin{cases} \Phi_{k,\text{OB}} (L/L_{k,\text{OB}})^{\beta_{\text{OB},1}}, & L \leq L_{k,\text{OB}}, \\ \Phi_{k,\text{OB}} (L/L_{k,\text{OB}})^{\beta_{\text{OB},2}}, & L > L_{k,\text{OB}}, \end{cases} \quad (11)$$

The existence of a knee, $L_{k,\text{OB}}$, is highly significant, with a $\gtrsim 7\sigma$ preference for a broken power law over a single power law ($p \simeq 5 \times 10^{-12}$).

Excluding the three faintest bins (16 LF remaining bins in total), a Monte Carlo perturbation of the binned LF yields faint- and bright-end slopes $\beta_{\text{OB},1} = -0.91 \pm 0.01$ and $\beta_{\text{OB},2} = -1.63 \pm 0.14$, with a knee at $\log_{10}(L_{k,\text{OB}}/L_\odot) = 5.0 \pm 0.1$. The corresponding normalisation at the knee is $\log_{10}\Phi_{k,\text{OB}} = 2.22 \pm 0.09$, i.e. $\Phi_{k,\text{OB}} = 167 \pm 37 \text{kpc}^{-3} \text{dex}^{-1}$. Using the *Modules for Experiments in Stellar Astrophysics* (MESA) Isochrones and Stellar Tracks (MIST; A. Dotter 2016; J. Choi et al. 2016), we derive a stellar mass-luminosity

relation, $L(m)$, by adopting the final stellar mass, m_f , as the mass coordinate of each evolutionary track, and taking as the corresponding luminosity L the time-averaged bolometric luminosity over the main-sequence phase. Using this $L(m)$ relation, the knee luminosity maps to a characteristic stellar mass of $m_{k,\text{OB}} = 25.0 \pm 2.4 M_\odot$. If the corresponding steepening of the stellar IMF corresponds to the IIM predictions in Section 2, the knee mass implies a characteristic star-forming cloud mass $M_k = m_{k,\text{OB}}/\epsilon_{\text{max}} \simeq 10^4 M_\odot$ for $\epsilon_{\text{max}} = 0.0025$.

As shown by the two dashed lines in the left panel of Figure 3, the two slopes of the LF are consistent with the analytic predictions in Section 3. For a constant star-formation rate and the Salpeter IMF slope, $s = 2.35$, and using $\delta = 1.62$ and $\gamma = 3.09$ (appropriate average values from the MIST tracks in the mass range $8\text{--}16 M_\odot$), equation (8) gives $\beta_{\text{OB}} = -0.96$, only slightly steeper than $\beta_{\text{OB},1}$ in the actual LF. At the bright end of the LF, adopting the value of $s_f = 3.35$ from equation (A6) for the steep section of the IMF, and $\delta = 0.55$ and $\gamma = 1.80$ (the average values from the MIST tracks in the mass range $40\text{--}80 M_\odot$), equation (8) gives $\beta_{\text{OB}} = -1.61$, consistent with the slope $\beta_{\text{OB},2}$ of the LF. The confirmation of the broken power-law OB-star LF lends strong support to a key aspect of the IIM, namely that the maximum stellar mass scales

with cloud mass. In the next Section we look for a signal of the growth law in the H II LF.

4.2. The Compact-H II-Region LF from the RMS Survey

Our LF of compact H II regions is based on the Red MSX Source (RMS) survey (S. L. Lumsden et al. 2013), which provides a homogeneously-selected, flux-limited sample of massive YSOs and H II regions across the Galactic plane, built from MSX and 2MASS colour cuts followed by extensive radio and mid-IR follow-up. Bolometric fluxes and luminosities for the RMS sources were derived by J. C. Mottram et al. (2011) from SED fits to the near- and mid-IR data (plus longer-wavelength photometry where available). The LF of the 832 compact H II regions in the luminosity range $3 \lesssim \log_{10}(L/L_\odot) \lesssim 6.5$ and distances $d \leq 18$ kpc (with selection criteria described in Appendix E and completeness correction method from Appendix C) is shown in the right panel of Fig. 3 (blue circles with 1σ Poisson error bars) together with the LF from M11 (gray squares). There is good agreement in both slopes and normalizations, which is expected because we adopt the same scale height of 39 pc as in M11, and our completeness correction is also similar, as mentioned in Appendix C. The figure also shows a broken power-law fit ($\gtrsim 7\sigma$ preference over a single power law as for the OB-star LF), based on the same parameterisation as in equation (11),

$$\Phi_{\text{H II}}(L) = \begin{cases} \Phi_{\text{k, H II}} (L/L_{\text{k, H II}})^{\beta_{\text{H II},1}}, & L \leq L_{\text{k, H II}}, \\ \Phi_{\text{k, H II}} (L/L_{\text{k, H II}})^{\beta_{\text{H II},2}}, & L > L_{\text{k, H II}}. \end{cases} \quad (12)$$

Excluding the first two low-luminosity bins (they will not be used in the following), a Monte Carlo perturbation of the binned LF yields faint- and bright-end slopes $\beta_{\text{H II},1} = -0.26 \pm 0.057$ and $\beta_{\text{H II},2} = -0.99 \pm 0.09$, with a knee at $\log_{10}(L_{\text{k, H II}}/L_\odot) = 4.6 \pm 0.1$, corresponding to a mass $m_{\text{k, H II}} \approx 18 M_\odot$. The corresponding normalisation at the knee is $\log_{10} \Phi_{\text{k, H II}} = 1.33 \pm 0.08$, i.e. $\Phi_{\text{k, H II}} = 22 \pm 4 \text{ kpc}^{-3} \text{ dex}^{-1}$.

The two slopes are consistent with the analytic predictions in Section 3, as shown by the two dashed lines in the right panel of Fig. 3. Assuming a Salpeter slope for the stellar IMF, $s = 2.35$, an effective $L(m)$ relation exponent $\gamma = 3.09$ (the average value from the MIST tracks in the mass range $8\text{--}16 M_\odot$), and a fiducial value of $\alpha = 0.5$, equation (9) gives $\beta_{\text{H II}} = -0.28$, almost identical to the slope $\beta_{\text{H II},1}$ of the actual LF. At the bright end of the LF, adopting the value of $s_f = 3.35$ from equation (A6) for the steep section of the IMF, $\gamma = 1.80$ (the average value from the MIST tracks in the mass range $40\text{--}80 M_\odot$), and the same fiducial value of $\alpha = 0.5$, equation (9) gives $\beta_{\text{H II}} = -1.03$, also almost identical to the slope $\beta_{\text{H II},2}$ of the LF.

4.3. The Relative Knee Position in the LFs

The knee mass corresponding to $L_{\text{k, H II}}$, $m_{\text{k, H II}} \approx 18 M_\odot$, should not be viewed as the *final* mass of the stars responsible for the H II regions of luminosity $L_{\text{k, H II}}$, because in our model the star powering the H II region has on average a mass smaller than m_f (the star is still growing). In addition, any star with final mass $\gtrsim m_{\text{k, H II}}$ may also contribute an H II region of that luminosity. This can be quantified using the linear growth law (equation (3)). At fixed instantaneous mass m , the relative contribution of stars with final mass $m_f \geq m$ scales as $p(m_f|m) \propto (dN/dm_f)(dt/dm) \propto m_f^{\alpha-s_f-1}$, where s_f is the steep IMF slope above the knee (equation (A6)). Since the knee is identified in logarithmic space, we characterize this distribution by its log-average, $\hat{m}_f(m) \equiv \exp[\langle \ln m_f \rangle_{p(m_f|m)}]$; evaluated at $m = m_{\text{k, H II}}$ it gives

$$m_{\text{k, OB}}^{(\text{geo})} = \exp\left[\frac{1}{s_f - \alpha}\right] m_{\text{k, H II}}, \quad (13)$$

or, in terms of luminosity,

$$L_{\text{k, OB}}^{(\text{geo})} = \exp\left[\frac{\gamma}{s_f - \alpha}\right] L_{\text{k, H II}}, \quad (14)$$

approximating the mass-luminosity relation locally as $L \propto m^\gamma$ around the knee. For $\alpha = 0.5$, $s_f = 3.35$, and $m_{\text{k, H II}} \approx 18 M_\odot$, equation (13) yields $m_{\text{k, OB}}^{(\text{geo})} \approx 25.6 M_\odot$, consistent with the knee mass $m_{\text{k, OB}} \simeq 25 M_\odot$ inferred from the OB-star LF. In luminosity, using $\gamma = 2.49$ (the average value in the mass range between 18 and $25 M_\odot$), and adopting $\log_{10}(L_{\text{k, H II}}/L_\odot) = 4.6$, we find $\log_{10}(L_{\text{k, OB}}^{(\text{geo})}/L_\odot) = 5.0$, consistent with the knee luminosity of the OB-star LF found earlier. Thus, the fact that $L_{\text{k, OB}} > L_{\text{k, H II}}$ is a non-trivial confirmation of our hypothesis that H II regions are powered by massive stars that are still forming.

5. MONTE-CARLO MODEL FOR THE LUMINOSITY FUNCTIONS

The analytic framework in Sections 2–3 shows that the pair of LFs $\{\phi_{\text{OB}}(L), \phi_{\text{H II}}(L)\}$ constrains the massive-star growth law, rather than directly measuring a “compact-H II-region lifetime at fixed L ”. In this interpretation, compact H II regions trace the ionising phase of accreting protostars, and their residence times are set by the mass-dependent formation time from IIM. We implement this as a Monte Carlo forward model for both LFs, to be compared with the observational LFs from the previous section (details of the model are given in Appendix F).

5.1. Constraints on the Growth-Law parameters

After finding the best-fit IMF from the comparison of the model and observed LFs of OB stars (step (i) in the inference pipeline of Appendix F), for each pair

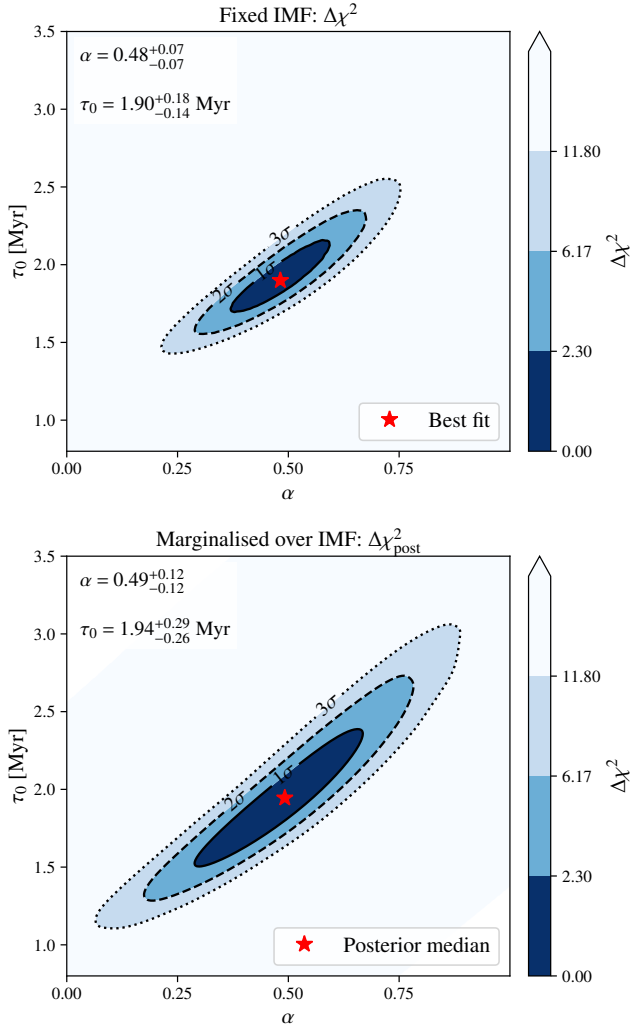


Figure 4. Constraints on the massive-star growth–law parameters α and τ_0 . *Top:* $\Delta\chi^2$ map from the fit of the compact H II-region LF using the best–fitting IMF. Filled contours show the joint 1, 2, and 3σ confidence regions for two parameters ($\Delta\chi^2 = 2.30, 6.17, 11.8$). The red star marks the best–fit point, with 1D profiled errors $\alpha = 0.48^{+0.07}_{-0.07}$ and $\tau_0 = 1.90^{+0.18}_{-0.14}$ Myr. *Bottom:* effective $\Delta\chi^2_{\text{post}}$ obtained after marginalising over the uncertainty in the broken–power–law IMF inferred from the observed OB-star LF. The red star indicates the posterior median, and the numbers in the top-left corner give the corresponding 68 per cent credible intervals, $\alpha = 0.49^{+0.12}_{-0.12}$ and $\tau_0 = 1.94^{+0.29}_{-0.26}$ Myr.

(α, τ_0) on a regular grid, we recompute the model H II-region LF and evaluate the χ^2 relative to the observed LF in log–space (step (ii) of the inference pipeline of Appendix F). For reference, the broken–power–law IMF parameters inferred from fitting the OB-star LF are

$$m_k = 23.0^{+1.7}_{-1.5} M_\odot, \quad s = 2.49^{+0.04}_{-0.04}, \quad s_f = 3.85^{+0.23}_{-0.21}, \quad (15)$$

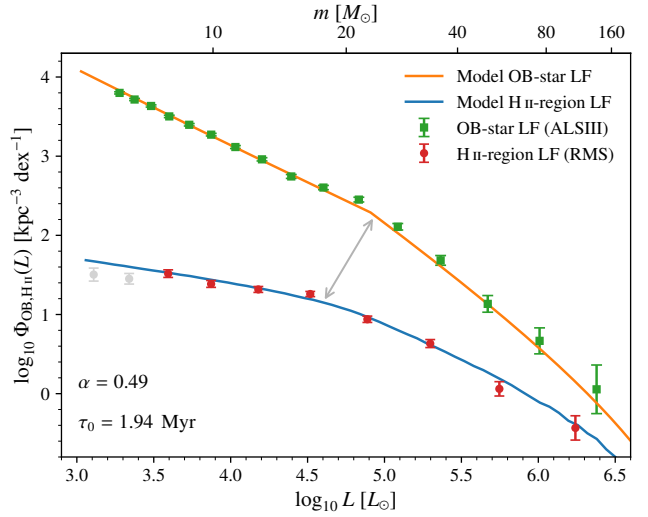


Figure 5. Comparison between the observed OB-star and compact H II-region LFs (green squares and red circles respectively) and the model predictions (orange and blue lines). Both model LFs shown here are derived from the same broken power–law IMF giving the best fit to the observed OB-star LF. The blue curve is the best fit to the observed H II-region LF corresponding to the best-fitting growth–law parameters $\alpha = 0.49$ and $\tau_0 = 1.94$ Myr. The double-headed arrow marks the approximate knee-to-knee correspondence, from the H II-region knee at $m_{k,\text{HII}} = 18 M_\odot$ to the OB-star knee at $m_{k,\text{OB}} = 25 M_\odot$.

where uncertainties denote 1σ confidence intervals from the OB-star LF χ^2 grid.

The top panel of Fig. 4 shows the resulting $\Delta\chi^2$ map in the (α, τ_0) plane (assuming the fixed best–fit IMF). The contours correspond to the joint 1, 2, and 3σ confidence regions for two parameters ($\Delta\chi^2 = 2.30, 6.17, 11.8$). The best–fitting model (red star) lies at

$$\alpha_{\text{fix}} = 0.48^{+0.07}_{-0.07}, \quad \tau_{0,\text{fix}} = 1.90^{+0.18}_{-0.14} \text{ Myr}, \quad (16)$$

where the quoted uncertainties are 1D profiled 1σ intervals obtained from the $\Delta\chi^2 = 1$ condition after minimising over the other parameter. The contours are elongated, reflecting the expected degeneracy: a steeper mass dependence (larger α) can be partially compensated by a longer normalisation timescale τ_0 .

To propagate the uncertainty of the IMF fit into the growth–law parameters, we repeat the H II-region LF fit over a Monte–Carlo ensemble of IMFs drawn from the original OB-star LF likelihood surface (step (iii) of the inference pipeline of Appendix F). Specifically, we sample the broken–power–law IMF parameter triplets (m_k, s, s_f) from the OB-star LF χ^2 grid, with sampling weights proportional to $\mathcal{L}_{\text{OB}} \propto \exp[-(\chi_{\text{OB}}^2 - \chi_{\text{OB,min}}^2)/2]$. Thus the IMF parameters are *not* refit or floated together with (α, τ_0) ; rather, their posterior uncertainty from the OB-star LF fit is propagated for

ward. For each IMF realisation we perform the full (α, τ_0) scan, identify the best-fitting point, and use the resulting ensemble of solutions to construct an effective posterior density $P(\alpha, \tau_0)$. The bottom panel of Fig. 4 shows the corresponding effective $\Delta\chi^2_{\text{post}}$ map, defined as $-2 \ln(P/P_{\text{max}})$, and the posterior median and 68 per cent credible intervals are

$$\alpha_{\text{post}} = 0.49^{+0.12}_{-0.12}, \quad \tau_{0,\text{post}} = 1.94^{+0.29}_{-0.26} \text{ Myr.} \quad (17)$$

The centroid of the allowed region in (α, τ_0) space is unchanged relative to the fixed-IMF case, while the confidence region is slightly broadened along the same degeneracy direction.

Figure 5 compares the observed OB-star and compact H II-region LFs (green squares and red circles) to the model predictions (orange and blue curves) adopting the best-fit growth-law parameters. The orange curve shows that the model OB-star LF reproduces the ALS III LF over the range $3.2 \lesssim \log(L/L_\odot) \lesssim 6.5$. Using the same IMF and adopting the best-fit growth-law parameters, the blue curve matches both the slope and the normalisation of the observed compact H II-region LF in the range $3.5 \lesssim \log(L/L_\odot) \lesssim 6.5$. As highlighted by the double-headed arrow in Fig. 5, the model simultaneously accounts for the different knee positions in the two LFs, providing an additional non-trivial consistency check of the interpretation developed in Section 4.2.

6. CONCLUSIONS

We have revisited the comparison between the LFs of compact H II regions and OB stars in the framework of the IIM, in which massive stars assemble over extended, mass-dependent formation timescales. Using revised observational LFs and a Monte-Carlo forward model that maps an IMF into both LFs through phase lifetimes and a growth law, we have obtained strong constraints on the growth-law parameters of the IIM. The main results are listed in the following.

1. We have derived updated, completeness-corrected LFs for compact H II regions (832 sources) and OB stars (9,607 sources) from the RMS and ALS III catalogues, respectively, which we then normalize to the same effective volume size.
2. The revised OB-star LF exhibits a statistically significant steepening above a knee luminosity $\log_{10}(L_{\text{k,OB}}/L_\odot) = 5.0 \pm 0.1$. This steepening cannot be explained by mass-dependent main-sequence lifetimes and therefore implies that the field IMF must also be a broken power law, as predicted by the model.

3. Fitting the OB-star LF with a broken power-law IMF yields $m_{\text{k}} = 23.0^{+1.7}_{-1.5} M_\odot$, $s = 2.49^{+0.04}_{-0.04}$, and $s_{\text{f}} = 3.85^{+0.23}_{-0.21}$.
4. The compact H II-region LF also shows a clear knee at $\log_{10}(L_{\text{k,HII}}/L_\odot) = 4.6 \pm 0.1 < \log_{10}(L_{\text{k,OB}}/L_\odot)$. The fainter knee luminosity compared to the OB-star LF confirms a key feature of the model: the compact H II emission is produced while $m < m_{\text{f}}$.
5. Jointly modelling the OB-star and compact H II-region LFs constrains the massive-star growth law $t_{\text{form}}(m_{\text{f}}) = \tau_0(m_{\text{f}}/m_0)^\alpha$. After marginalising over the IMF uncertainty, we obtain $\alpha = 0.49^{+0.12}_{-0.12}$ and $\tau_0 = 1.94^{+0.29}_{-0.26}$ Myr (for $m_0 = 60 M_\odot$), consistent with the IIM expectation of $\alpha \simeq 0.5$ and implying formation times of $\approx 0.7 - 2.4$ Myr for masses of $\approx 8 - 100 M_\odot$.
6. In this framework, the long “lifetimes” inferred from the LF comparisons are naturally reinterpreted as evidence that compact H II regions trace an extended phase of ongoing mass assembly in which accretion and photoionization co-exist, rather than as an expansion/confinement timescale problem.

We stress that while α is expected to be a universal property of supersonic turbulence, τ_0 may be smaller in more extreme environments with higher gas (surface) densities (see the scaling derived in M. Gieles et al. 2025). The IMF parameters may also vary, but we do not emphasize them here because the growth law is constrained primarily by the relative shapes of the LFs, largely independent of the underlying IMF.

Future work should incorporate stellar-evolution tracks computed with accretion rates consistent with the inferred growth law, to refine estimates of m_{ion} (including its dependence on m_{f}) and $t_{\text{MS}}(m_{\text{f}})$, which is likely shorter at the highest masses because core hydrogen burning starts before the star reaches m_{f} . It will also be useful to test the impact of multiple OB stars powering individual compact H II regions and to improve the OB-star LF with a more careful treatment of the degeneracy between effective temperature and extinction. Nonetheless, we do not expect such refinements to alter the main qualitative conclusion that massive stars form over Myr timescales that increase with their final mass.

ACKNOWLEDGMENTS

PP acknowledges support by the US National Science Foundation under Grant AST 2408023. MG acknowledge financial support from the grants PID2024-155720NB-I00, CEX2024-001451-M funded by MCIN/AEI/10.13039/501100011033 (State Agency for Research of the Spanish Ministry of Science and Innovation).

APPENDIX

A. THE UPPER END OF THE FIELD IMF

Because m_{\max} is proportional to the total mass of the star-forming cloud (equation 4), the *field* IMF, which is the outcome of star-formation from many clouds with different mass M , cannot be a single power law: it must steepen at masses where the finite m_{\max} of typical clouds becomes important. To model this, we introduce a *knee mass* M_k , defined as the typical maximum stellar mass in the lowest-mass clouds capable of forming stars, corresponds to a characteristic cloud mass

$$M_k \equiv \frac{m_k}{\varepsilon_{\max}}. \quad (\text{A1})$$

For the purpose of this derivation we simply assume that clouds with mass $< M_k$ do not contribute to star formation due to their large virial parameters (e.g. M. H. Heyer et al. 2001; N. J. Evans et al. 2021) and thus negligible star-formation rate (P. Padoan & Å. Nordlund 2011; P. Padoan et al. 2012, 2017). Above M_k , we assume that star-forming clouds follow a power-law mass function,

$$\frac{dN_{\text{cloud}}}{dM} = C_{\text{cloud}} M^{-\beta}, \quad (\text{A2})$$

as well documented for Galactic molecular clouds (e.g. M. H. Heyer et al. 2001; J. Roman-Duval et al. 2010; M.-A. Miville-Deschénes et al. 2017; D. Colombo et al. 2019) and for molecular clouds in nearby galaxies (e.g. E. Rosolowsky 2005; P. Gratier et al. 2012; D. Colombo et al. 2014; D. Utomo et al. 2015; C. M. Faesi et al. 2018; E. Rosolowsky et al. 2021). The characteristic value of the exponent is $\beta \simeq 2$, but with significant variations in different environments (often larger at larger galactocentric distances or in inter-arm regions).

To evaluate the steepening, we assume that within a given cloud the stellar IMF (the distribution of final stellar masses, m_f) at high mass is a power law,

$$\xi(m_f) = \frac{dN}{dm_f} \propto m_f^{-s}, \quad (\text{A3})$$

truncated at the maximum mass $m_{\max}(M) = \varepsilon_{\max}M$. The *field* IMF at mass m_f is then obtained by summing over all clouds that can host such stars, namely all clouds with $M \geq m_f/\varepsilon_{\max}$:

$$\xi_{\text{field}}(m_f) \propto \xi(m_f) \int_{M \geq m_f/\varepsilon_{\max}} M^{-\beta} dM. \quad (\text{A4})$$

Thus, for $m_f \gtrsim m_k$ we obtain

$$\xi_{\text{field}}(m_f) \propto m_f^{-s} m_f^{1-\beta} = m_f^{-(s+\beta-1)}, \quad (\text{A5})$$

so the effective high-mass slope of the field IMF is

$$s_f = s + \beta - 1 \simeq 3.35, \quad (\text{A6})$$

where the approximate value assumes $\beta \simeq 2$ and $s \simeq 2.35$ (E. E. Salpeter 1955).⁶

B. THE SLOPE OF THE H II-REGION LF

As a star grows, it eventually becomes massive enough to ionize its surroundings. We define an ionization threshold m_{ion} , such that a star with instantaneous mass $m(t; m_f) \geq m_{\text{ion}}$ drives a compact H II region. With the linear growth law (equation (3)), the ionizing phase for a star of final mass $m_f > m_{\text{ion}}$ begins when $m(t; m_f) = m_{\text{ion}}$ and ends when $m(t; m_f) = m_f$. The corresponding start time is

$$t_{\text{ion}}(m_f) = t_{\text{form}}(m_f) \frac{m_{\text{ion}}}{m_f}, \quad (\text{B7})$$

so the duration of the compact H II phase is

$$t_{\text{H II}}(m_f) = t_{\text{form}}(m_f) - t_{\text{ion}}(m_f) = t_{\text{form}}(m_f) \left[1 - \frac{m_{\text{ion}}}{m_f} \right]. \quad (\text{B8})$$

⁶ The steepening of the field IMF due to a dependence of the maximum stellar mass on the cluster mass was discussed in C. Weidner & P. Kroupa (2006). However, the steepening is less pronounced and model dependent, with the largest value of $s_f = 3.0$ starting from $\beta = 2.35$ (where β is the slope of the cluster mass function), and the steepening applies to all stars above $1 M_{\odot}$.

The growth law (equation (3)) implies a constant accretion rate along each track,

$$\frac{dm}{dt} = \frac{m_f}{t_{\text{form}}(m_f)}. \quad (\text{B9})$$

During the compact H II phase the instantaneous mass runs from $m = m_{\text{ion}}$ to $m = m_f$, so at fixed m_f the time spent in a mass interval dm is $dt = t_{\text{form}}(m_f) dm/m_f$. The total compact H II lifetime for that star is $t_{\text{H II}}(m_f)$, from equation (B8), so the fraction of the compact H II lifetime spent in dm is $dt/t_{\text{H II}}(m_f)$. Therefore, in a steady state with a constant star-formation rate, the number density of compact H II regions contributed by stars of final mass m_f in the interval $[m, m + dm]$ is

$$dn_{\text{H II}}(m | m_f) \propto \xi(m_f) t_{\text{H II}}(m_f) \frac{dt}{t_{\text{H II}}(m_f)} \propto \xi(m_f) \frac{t_{\text{form}}(m_f)}{m_f} dm. \quad (\text{B10})$$

The factor $t_{\text{H II}}(m_f)$ cancels out, so the result is independent of the choice of m_{ion} apart from the requirement that $m \geq m_{\text{ion}}$.

Integrating over all final masses that can reach a given instantaneous mass m then gives the steady-state number density per unit mass,

$$n_{\text{H II}}(m) \propto \int_m^{m_{\text{max}}} m_f^{-s} \frac{t_{\text{form}}(m_f)}{m_f} dm_f, \quad (m \geq m_{\text{ion}}), \quad (\text{B11})$$

where m_{max} is the upper cutoff of the IMF in a given cloud. Substituting $t_{\text{form}}(m_f) \propto m_f^\alpha$ yields an integrand $\propto m_f^{\alpha-s-1}$, so that

$$n_{\text{H II}}(m) \propto \frac{m_{\text{max}}^{\alpha-s} - m^{\alpha-s}}{\alpha - s}, \quad (\alpha \neq s, m \geq m_{\text{ion}}). \quad (\text{B12})$$

This expression explicitly retains both integration limits and shows that, in general, the compact H II LF is an integral transform of the IMF and the growth law, rather than a pure power law.

For realistic parameters $\alpha < s$ the exponent $\alpha - s$ is negative. For masses well inside the allowed range, $m_{\text{ion}} \lesssim m \ll m_{\text{max}}$, the second term in the numerator dominates in absolute value and the scaling reduces to

$$n_{\text{H II}}(m) \propto m^{\alpha-s}. \quad (\text{B13})$$

Per dex in instantaneous mass this becomes

$$\frac{dn_{\text{H II}}}{d \log m} \propto m n_{\text{H II}}(m) \propto m^{1+\alpha-s}. \quad (\text{B14})$$

Approximating the compact H II region luminosity as that of the ionizing star, $L \propto m^\gamma$, we obtain

$$\phi_{\text{H II}}(L) \propto L^{\beta_{\text{H II}}}, \quad \beta_{\text{H II}} = \frac{1 + \alpha - s}{\gamma}, \quad (\text{B15})$$

which can be applied separately to both the shallower range with $s = 2.35$ and the steeper range with $s = s_f$ (equation A6).

C. COMPLETENESS CORRECTION AND RELATIVE NORMALIZATION OF THE LFS

C.1. *Empirical Effective-Volume Completeness Correction*

Our completeness correction is based on an empirical estimate of the *effective survey volume* as a function of luminosity. The key idea is that, at fixed luminosity, the inferred space density should be approximately independent of the adopted heliocentric volume as long as the catalogue remains effectively complete at that luminosity; when the adopted volume extends beyond the effective completeness limit, the inferred density decreases because the sampled volume grows faster than the number of detected sources. We therefore infer, for each luminosity, an effective volume directly from the data by identifying the heliocentric volume that maximizes the inferred number density, without assuming a parametric selection function. Under the standard assumption that the LF *shape* is independent of distance, this construction can accommodate genuine distance-dependent normalization variations due to Galactic structure because it does not impose any parametric relation between luminosity and distance.

For a heliocentric distance limit d we define a distance-limited LF

$$\phi(L; d) \equiv \frac{dN(L; d)}{d \log_{10} L} \frac{1}{V(d)}, \quad V(d) = 2h \pi d^2, \quad (\text{C16})$$

where we adopt an exponential vertical distribution with scale height h . We then define an effective maximum distance $d_{\text{eff}}(L)$ (equivalently $V_{\text{eff}}(L) = V[d_{\text{eff}}(L)]$) by

$$\phi(L; d_{\text{eff}}(L)) = \max_d \phi(L; d). \quad (\text{C17})$$

In principle, one could evaluate the LF directly as $\phi(L; d_{\text{eff}}(L))$. In practice, $d_{\text{eff}}(L)$ is smaller at the faint end, so this would use only a subset of the catalogue and yield relatively large Poisson uncertainties there. We therefore use the effective-volume construction primarily to estimate a smooth, luminosity-dependent completeness correction for a single large reference sample that contains many sources.

Specifically, we compute a “raw” LF $\phi_{\text{raw}}(L; d_0)$ in a fixed large distance limit d_0 (6 kpc for OB stars and 18 kpc for compact H II regions). We then estimate an empirical completeness factor on a coarser luminosity grid $\{L_k\}$ by comparing the maximum inferred density in each coarse bin to the raw density in the same bin,

$$\hat{C}_k \equiv \frac{\max_d \phi(L_k; d)}{\phi_{\text{raw}}(L_k; d_0)} \geq 1. \quad (\text{C18})$$

Treating completeness as a smooth function of L , we fit/interpolate the discrete set $\{\hat{C}_k\}$ to obtain a continuous estimate $\hat{C}(L)$, which we apply to the finely binned raw LF:

$$\phi_{\text{corr}}(L) = \hat{C}(L) \phi_{\text{raw}}(L; d_0), \quad (\text{C19})$$

with Poisson uncertainties from $\phi_{\text{raw}}(L; d_0)$ scaled by the same factor. For compact H II regions, we find $\hat{C}(L) \approx 2$ at $\log_{10}(L/L_\odot) \sim 4.0$ and $\hat{C}(L) \approx 10$ at $\log_{10}(L/L_\odot) \sim 3.0$, in good agreement with the corresponding correction in M11 at the same luminosities.

C.2. Renormalization of the Compact-H II-Region LF

Because the LF normalization can vary with heliocentric distance (and Galactocentric radius) due to large-scale structure in the star-forming disc, we place the OB-star and compact H II-region LFs on a common *effective local-volume* scale. We do this by choosing a reference luminosity L_{ref} near the middle of the dynamic range, bright enough to be sampled over a reasonably large volume but not so bright that the counts are dominated by small-number statistics; we adopt $\log_{10}(L_{\text{ref}}/L_\odot) \simeq 5.0$.

We then define the local distance scale directly from the effective-volume definition in equation (C17). Specifically, for the OB-star LF we set

$$d_{\text{loc}} \equiv d_{\text{eff,OB}}(L_{\text{ref}}), \quad (\text{C20})$$

i.e. the distance limit that maximizes the inferred OB-star number density at L_{ref} . We find $d_{\text{loc}} = 2.75$ kpc. This choice is supported empirically by the OB-star distance distribution, which shows a pronounced decline just beyond that distance, and by the fact that $d_{\text{eff,OB}}(L)$ varies only weakly around L_{ref} .

We renormalize the corrected compact-H II-region LF, $\phi_{\text{H II}}^{\text{corr}}(L)$, to the same local-volume scale by comparing its normalization at L_{ref} to the compact-H II-region number density measured within d_{loc} . Their ratio defines a constant rescaling factor

$$f \equiv \frac{\phi_{\text{H II}}(L_{\text{ref}}; d_{\text{loc}})}{\phi_{\text{H II}}^{\text{corr}}(L_{\text{ref}})}, \quad (\text{C21})$$

for which we obtain $f = 0.75$. Since $d_{\text{eff,H II}}(L_{\text{ref}}) > d_{\text{loc}}$ (compact H II regions are detected to greater distances), one would naively expect $\phi_{\text{H II}}(L_{\text{ref}}; d)$ to be approximately independent of d for $d \lesssim d_{\text{eff,H II}}(L_{\text{ref}})$. The fact that $\phi_{\text{H II}}(L_{\text{ref}}; d_{\text{loc}})$ is smaller than $\phi_{\text{H II}}^{\text{corr}}(L_{\text{ref}})$ therefore indicates that the normalization varies with distance, consistent with large-scale Galactic structure. In our modelling we therefore multiply the completeness-corrected compact H II-region LF by f , so that both observational LFs represent number densities normalized to the same effective local volume.

D. SOURCE SELECTION AND BOLOMETRIC LUMINOSITIES FROM THE ALS III CATALOG

Starting from the ALS III list of candidate luminous stars we retain only objects with a finite *Gaia* median distance d_{med} , the good astrometry flag **Aflag** = G, and renormalised unit weight error **RUWE** < 1.4, and consider stars with reliable *Gaia* distances out to $d_{\text{med}} \leq 6$ kpc. The ALS III catalog contains stars out to a distance of ≈ 19 kpc, but with our distance cut we still retain 95.3% of stars with $\log_{10}(L/L_\odot) \geq 3.0$. Apparent G-band magnitudes are corrected

for extinction using the DR3 GSP-Phot extinction A_G (R. Andrae et al. 2023) when available (or $A_G = 0$ otherwise), yielding

$$M_G = G - 5 \log_{10} \left(\frac{d_{\text{med}}}{10 \text{ pc}} \right) - A_G. \quad (\text{D22})$$

For stars with secure O-star spectral classifications in the GOS catalogue we adopt the updated empirical spectral-type–temperature calibration of G. Holgado et al. (2025), which provides T_{eff} as a function of spectral subtype and luminosity class (V, III, I) over the subtype range O4–O9.7. For these subtypes we take T_{eff} from their Table D1 and convert to *Gaia* G-band bolometric corrections, BC_G , by interpolating the YBC grid of bolometric corrections based on TLUSTY OB-star model atmospheres in the *Gaia* passbands (Y. Chen et al. 2019). For the subtype range O2–O3.5 we adopt the updated empirical spectral-type–temperature calibration of F. Martins et al. (2005) and derive BC_G in the same way via the YBC *Gaia* G-band grid.

For the B stars (7,347 stars in our final LF) there is no equivalent GOS spectral classification. Instead we adopt the *Gaia* DR3 astrophysical-parameter T_{eff} and compute BC_G from T_{eff} using the OBA-star G-band bolometric-correction prescriptions of M. G. Pedersen (2020). For stars without a published *Gaia* T_{eff} we assign a single BC_G corresponding to $T_{\text{eff}} \simeq 2 \times 10^4$ K in the M. G. Pedersen (2020) calibration, appropriate for mid-B stars, and adequate at the lower-luminosity end of the LF, where most of the missing *Gaia* T_{eff} stars reside. The bolometric luminosity then follows from

$$\log_{10} \left(\frac{L}{L_\odot} \right) = -0.4 (M_G + BC_G - M_{\text{bol},\odot}), \quad (\text{D23})$$

with $M_{\text{bol},\odot} = 4.74$.

E. SOURCE SELECTION FROM THE RMS CATALOG

Starting from the full RMS catalogue (2798 objects in the VizieR table), we select all sources whose `Type` flag is “HII region”, corresponding to compact or ultra-compact H II regions as defined by S. L. Lumsden et al. (2013). Objects classified as “diffuse HII region” or as ambiguous “HII/YSO” are excluded. We then require a finite, positive bolometric luminosity L_{bol} and heliocentric distance d ; sources lacking either quantity, or with obviously spurious values, are removed. This yields a working sample of $N_{\text{HII}} = 885$ compact H II regions with reliable (L_{bol}, d) pairs.

F. MONTE–CARLO MODEL FOR THE LUMINOSITY FUNCTIONS

The Monte Carlo model does not introduce any new physics beyond what was already assumed in Sections 2–3. Its inputs are:

- a broken-power-law field IMF with knee mass m_k and slopes s and s_f below and above the knee;
- a formation-time law $t_{\text{form}}(m_f)$ of the form of equation (2), where α and τ_0 are the growth-law parameters to be constrained;
- a growth track $m(t; m_f)$ that increases linearly in mass from a seed mass $m_{\text{seed}} = 1 M_\odot$ to the final mass m_f over $t_{\text{form}}(m_f)$, as in equation (3);
- a definition of the compact H II-region phase as the portion of each track between $m = m_{\text{ion}}$ and $m = m_f$, where $m_{\text{ion}} = 5.5 M_\odot$ marks the onset of the ionising output (Appendix B);
- a stellar mass–luminosity relation $L(m)$ and a main-sequence lifetime-mass relation $t_{\text{MS}}(m)$ based on the MIST evolutionary tracks, where L is the average value during the main sequence, and t_{MS} is the main-sequence duration from the tracks;
- the observational LFs from Sections 4.

F.1. Forward Model: from an IMF and Growth Law to the LFs

Given a choice of IMF and growth-law parameters (fixed m_k , s , s_f, α, τ_0), we evaluate a forward model for the pair of LFs $\{\phi_{\text{OB}}(L), \phi_{\text{H II}}(L)\}$. Assuming a constant star-formation rate, the number of objects observed in a given evolutionary phase is proportional to the birthrate into that phase times its duration. Thus, for stars of final mass m_f , the contribution to the compact H II-region LF scales as $\xi(m_f) t_{\text{H II}}(m_f)$, while the contribution to the OB-star LF scales as $\xi(m_f) t_{\text{MS}}(m_f)$. We implement this with a two-level Monte Carlo sampling. First, we draw a large sample of final masses m_f from the steady-state instantaneous distribution appropriate to each phase. For a phase X (compact

H II region or main-sequence OB star), the number of objects present at any instant is proportional to the birthrate into that phase times its duration, so we sample

$$p_X(m_f) = \frac{\xi(m_f) t_X(m_f)}{\int \xi(m_f) t_X(m_f) dm_f}. \quad (\text{F24})$$

Second, for the H II-region LF ($X = \text{H II}$) we draw an instantaneous stellar mass m along the ionising portion of the growth track, $m_{\text{ion}} \leq m \leq m_f$ (Fig. 2). Since equation (3) implies a constant accretion rate, sampling uniformly in time over the compact H II phase is equivalent to sampling uniformly in mass. Each sampled mass is mapped to a bolometric luminosity using $L(m)$, and the resulting luminosity sample is accumulated into a model H II-region LF. The OB-star LF is computed by sampling m_f from $p_{\text{MS}}(m_f) \propto \xi(m_f) t_{\text{MS}}(m_f)$ and mapping m_f directly to L with the same $L(m)$ relation.

F.2. Inference Pipeline

The inference pipeline built around the forward model consists of three numerical steps. (i) We fit a broken-power-law IMF to the ALS III OB-star LF by constructing a χ^2 grid over (m_k, s, s_f) . The best-fitting IMF shape and its normalisation define a fiducial birthrate. (ii) Holding the IMF fixed to this fiducial solution, we evaluate the compact H II-region LF on a grid of growth-law parameters (α, τ_0) and compare it to the observed LF in logarithmic space, yielding the best-fitting (α, τ_0) for the fixed IMF. (iii) We propagate IMF uncertainties by drawing IMF parameters from the (m_k, s, s_f) χ^2 grid and repeating step (ii) for each draw, thereby mapping the allowed region in (m_k, s, s_f) into an allowed region in (α, τ_0) .

REFERENCES

Andrae, R., Fouesneau, M., Sordo, R., et al. 2023, A&A, 674, A27, doi: [10.1051/0004-6361/202243813](https://doi.org/10.1051/0004-6361/202243813)

Bonnell, I. A., Bate, M. R., Clarke, C. J., & Pringle, J. E. 2001a, MNRAS, 323, 785, doi: [10.1046/j.1365-8711.2001.04270.x](https://doi.org/10.1046/j.1365-8711.2001.04270.x)

Bonnell, I. A., Clarke, C. J., Bate, M. R., & Pringle, J. E. 2001b, MNRAS, 324, 573, doi: [10.1046/j.1365-8711.2001.04311.x](https://doi.org/10.1046/j.1365-8711.2001.04311.x)

Bunker, A. J., Saxena, A., Cameron, A. J., et al. 2023, A&A, 677, A88, doi: [10.1051/0004-6361/202346159](https://doi.org/10.1051/0004-6361/202346159)

Castellano, M., Napolitano, L., Fontana, A., et al. 2024, ApJ, 972, 143, doi: [10.3847/1538-4357/ad5f88](https://doi.org/10.3847/1538-4357/ad5f88)

Charbonnel, C., Schaefer, D., Prantzos, N., et al. 2023, A&A, 673, L7, doi: [10.1051/0004-6361/202346410](https://doi.org/10.1051/0004-6361/202346410)

Chen, Y., Girardi, L., Fu, X., et al. 2019, Astronomy & Astrophysics, 632, A105, doi: [10.1051/0004-6361/201936612](https://doi.org/10.1051/0004-6361/201936612)

Choi, J., Dotter, A., Conroy, C., et al. 2016, The Astrophysical Journal, 823, 102, doi: [10.3847/0004-637X/823/2/102](https://doi.org/10.3847/0004-637X/823/2/102)

Churchwell, E. 2002, ARA&A, 40, 27

Colombo, D., Hughes, A., Schinnerer, E., et al. 2014, ApJ, 784, 3, doi: [10.1088/0004-637X/784/1/3](https://doi.org/10.1088/0004-637X/784/1/3)

Colombo, D., Rosolowsky, E., Duarte-Cabral, A., et al. 2019, MNRAS, 483, 4291, doi: [10.1093/mnras/sty3283](https://doi.org/10.1093/mnras/sty3283)

Dotter, A. 2016, The Astrophysical Journal Supplement Series, 222, 8, doi: [10.3847/0067-0049/222/1/8](https://doi.org/10.3847/0067-0049/222/1/8)

Ebihara, S., Fujii, M. S., Saitoh, T. R., et al. 2026, arXiv e-prints, arXiv:2601.04344, doi: [10.48550/arXiv.2601.04344](https://doi.org/10.48550/arXiv.2601.04344)

Evans, II, N. J., Heyer, M., Miville-Deschénes, M.-A., Nguyen-Luong, Q., & Merello, M. 2021, ApJ, 920, 126, doi: [10.3847/1538-4357/ac1425](https://doi.org/10.3847/1538-4357/ac1425)

Faesi, C. M., Lada, C. J., & Forbrich, J. 2018, ApJ, 857, 19, doi: [10.3847/1538-4357/aaad60](https://doi.org/10.3847/1538-4357/aaad60)

Gaia Collaboration, Vallenari, A., Brown, A. G. A., et al. 2023, Astronomy & Astrophysics, 674, A1, doi: [10.1051/0004-6361/202243940](https://doi.org/10.1051/0004-6361/202243940)

Galván-Madrid, R., Peters, T., Keto, E. R., et al. 2011, Monthly Notices of the Royal Astronomical Society, 416, 1033, doi: [10.1111/j.1365-2966.2011.19101.x](https://doi.org/10.1111/j.1365-2966.2011.19101.x)

Gieles, M., Padoan, P., Charbonnel, C., Vink, J. S., & Ramírez-Galeano, L. 2025, Monthly Notices of the Royal Astronomical Society, 544, 483, doi: [10.1093/mnras/staf1314](https://doi.org/10.1093/mnras/staf1314)

Gratier, P., Braine, J., Rodriguez-Fernandez, N. J., et al. 2012, A&A, 542, A108, doi: [10.1051/0004-6361/201116612](https://doi.org/10.1051/0004-6361/201116612)

Heyer, M. H., Carpenter, J. M., & Snell, R. L. 2001, ApJ, 551, 852, doi: [10.1086/320218](https://doi.org/10.1086/320218)

Holgado, G., Simón-Díaz, S., & Herrero, A. 2025, Astronomy & Astrophysics, 703, A175, doi: [10.1051/0004-6361/202556713](https://doi.org/10.1051/0004-6361/202556713)

Hollenbach, D., Johnstone, D., Lizano, S., & Shu, F. 1994, ApJ, 428, 654, doi: [10.1086/174276](https://doi.org/10.1086/174276)

Keto, E. 2002, *The Astrophysical Journal*, 580, 980, doi: [10.1086/343794](https://doi.org/10.1086/343794)

Lumsden, S. L., Hoare, M. G., Urquhart, J. S., et al. 2013, *Astrophysical Journal Supplement Series*, 208, 11

Maíz-Apellániz, J., Walborn, N. R., Galué, H. Á., & Wei, L. H. 2004, *The Astrophysical Journal Supplement Series*, 151, 103, doi: [10.1086/381377](https://doi.org/10.1086/381377)

Martins, F., Schaefer, D., & Hillier, D. J. 2005, *Astronomy and Astrophysics*, 436, 1049, doi: [10.1051/0004-6361:20042386](https://doi.org/10.1051/0004-6361:20042386)

McKee, C. F., & Tan, J. C. 2002, *Nature*, 416, 59, doi: [10.1038/416059a](https://doi.org/10.1038/416059a)

McKee, C. F., & Tan, J. C. 2003, *ApJ*, 585, 850, doi: [10.1086/346149](https://doi.org/10.1086/346149)

Miville-Deschénes, M.-A., Murray, N., & Lee, E. J. 2017, *ApJ*, 834, 57, doi: [10.3847/1538-4357/834/1/57](https://doi.org/10.3847/1538-4357/834/1/57)

Mottram, J. C., Hoare, M. G., Lumsden, S. L., et al. 2011, *Astronomy & Astrophysics*, 525, A149, doi: [10.1051/0004-6361/201014591](https://doi.org/10.1051/0004-6361/201014591)

Naidu, R. P., Oesch, P. A., Brammer, G., et al. 2025, arXiv e-prints, arXiv:2505.11263, doi: [10.48550/arXiv.2505.11263](https://doi.org/10.48550/arXiv.2505.11263)

Nony, T., Galván-Madrid, R., Brouillet, N., et al. 2024, *A&A*, 687, A84, doi: [10.1051/0004-6361/202449279](https://doi.org/10.1051/0004-6361/202449279)

Padoan, P., Haugbølle, T., & Nordlund, Å. 2012, *ApJL*, 759, L27, doi: [10.1088/2041-8205/759/2/L27](https://doi.org/10.1088/2041-8205/759/2/L27)

Padoan, P., Haugbølle, T., Nordlund, Å., & Frimann, S. 2017, *ApJ*, 840, 48, doi: [10.3847/1538-4357/aa6afa](https://doi.org/10.3847/1538-4357/aa6afa)

Padoan, P., & Nordlund, Å. 2011, *ApJ*, 730, 40, doi: [10.1088/0004-637X/730/1/40](https://doi.org/10.1088/0004-637X/730/1/40)

Padoan, P., Pan, L., Juvela, M., Haugbølle, T., & Nordlund, Å. 2020, *ApJ*, 900, 82, doi: [10.3847/1538-4357/abaa47](https://doi.org/10.3847/1538-4357/abaa47)

Pantaleoni González, M., Maíz Apellániz, J., Barbá, R. H., et al. 2025, *MNRAS*, 543, 63, doi: [10.1093/mnras/staf1409](https://doi.org/10.1093/mnras/staf1409)

Pantaleoni González, M., Reed, B. C., Maíz Apellániz, J., & Barbá, R. H. 2021, *MNRAS*, 504, 2968, doi: [10.1093/mnras/stab688](https://doi.org/10.1093/mnras/stab688)

Pedersen, M. G. 2020, *Monthly Notices of the Royal Astronomical Society*, 495, 3909

Peters, T., Banerjee, R., Klessen, R. S., et al. 2010, *The Astrophysical Journal*, 711, 1017, doi: [10.1088/0004-637X/711/2/1017](https://doi.org/10.1088/0004-637X/711/2/1017)

Reed, B. C. 2003, *The Astronomical Journal*, 125, 2531, doi: [10.1086/374771](https://doi.org/10.1086/374771)

Reed, B. C. 2005, *AJ*, 130, 1652

Roman-Duval, J., Jackson, J. M., Heyer, M., Rathborne, J., & Simon, R. 2010, *ApJ*, 723, 492, doi: [10.1088/0004-637X/723/1/492](https://doi.org/10.1088/0004-637X/723/1/492)

Rosolowsky, E. 2005, *PASP*, 117, 1403, doi: [10.1086/497582](https://doi.org/10.1086/497582)

Rosolowsky, E., Hughes, A., Leroy, A. K., et al. 2021, *MNRAS*, 502, 1218, doi: [10.1093/mnras/stab085](https://doi.org/10.1093/mnras/stab085)

Salpeter, E. E. 1955, *ApJ*, 121, 161

Urquhart, J. S., Busfield, A. L., Hoare, M. G., et al. 2008, *Astronomy & Astrophysics*, 487, 253, doi: [10.1051/0004-6361:200809415](https://doi.org/10.1051/0004-6361:200809415)

Utomo, D., Blitz, L., Davis, T., et al. 2015, *ApJ*, 803, 16, doi: [10.1088/0004-637X/803/1/16](https://doi.org/10.1088/0004-637X/803/1/16)

Weidner, C., & Kroupa, P. 2006, *MNRAS*, 365, 1333, doi: [10.1111/j.1365-2966.2005.09824.x](https://doi.org/10.1111/j.1365-2966.2005.09824.x)

Wood, D. O. S., & Churchwell, E. 1989a, *ApJS*, 69, 831, doi: [10.1086/191329](https://doi.org/10.1086/191329)

Wood, D. O. S., & Churchwell, E. 1989b, *ApJ*, 340, 265, doi: [10.1086/167390](https://doi.org/10.1086/167390)